J. Fluid Mech. (2013), *vol.* 728, *pp.* 340–361. © Cambridge University Press 2013
doi:10.1017/jfm.2013.274

Two-dimensional vortex structures in the bottom boundary layer of progressive and solitary waves

Pietro Scandura†

Department of Civil and Environmental Engineering, University of Catania, Viale A. Doria 6, 95125, Italy

(Received 21 July 2012; revised 28 February 2013; accepted 24 May 2013;
first published online 9 July 2013)

The two-dimensional vortices characterizing the bottom boundary layer of both progressive and solitary waves, recently discovered by experimental flow visualizations and referred to as vortex tubes, are studied by numerical solution of the governing equations. In the case of progressive waves, the Reynolds numbers investigated belong to the subcritical range, according to Floquet linear stability theory. In such a range the periodic generation of strictly two-dimensional vortex structures is not a self-sustaining phenomenon, being the presence of appropriate ambient disturbances necessary to excite certain modes through a receptivity mechanism. In a physical experiment such disturbances may arise from several coexisting sources, among which the most likely is roughness. Therefore, in the present numerical simulations, wall imperfections of small amplitude are introduced as a source of disturbances for both types of wave, but from a macroscopic point of view the wall can be regarded as flat. The simulations show that even wall imperfections of small amplitude may cause flow instability and lead to the appearance of vortex tubes. These vortices, in turn, interact with a vortex layer adjacent to the wall and characterized by vorticity opposite to that of the vortex tubes. In a first stage such interaction gives rise to corrugation of the vortex layer and this affects the spatial distribution of the wall shear stress. In a second stage the vortex layer rolls up and pairs of counter-rotating vortices are generated, which leave the bottom because of the self-induced velocity.

Key words: boundary layers, instability, surface gravity waves

1. Introduction

The boundary layer generated by an unsteady pressure gradient near a flat wall is the archetype of a bottom boundary layer under surface gravity waves. This paper is devoted to the analysis of the vortex structures that may appear in such a boundary layer in the case of progressive or solitary waves. The topic is of interest for the quantification of sediment transport, which requires detailed knowledge of the hydrodynamic processes that occur close to the sea bed. In this section we first review the literature concerning progressive waves and then the literature on solitary waves.

The boundary layer at the bottom of a progressive wave, at the first order of approximation in the wave slope, is equivalent to that generated by a sinusoidally time-varying pressure gradient. Such a boundary layer is known as the Stokes layer,

† Email address for correspondence: pscandu@dica.unict.it

https://doi.org/10.1017/jfm.2013.274 Published online by Cambridge University Press

and has received considerable attention, being of interest in water wave mechanics as well as in physiological and industrial flows.

The Reynolds number R_δ of the Stokes layer is defined by $u_0^*\delta^*/\nu^*$, where u_0^* is the amplitude of the velocity oscillations in the irrotational region, δ^* is the conventional thickness of the boundary layer, given by $\sqrt{2\nu^*/\sigma^*}$, ν^* is the kinematic viscosity and σ^* is the angular frequency of fluid oscillations. A star is used to denote dimensional quantities.

In the past, several experimental investigations have been aimed at determining the value of R_δ for which transition from the laminar to the turbulence regime takes place. Values of the critical Reynolds number in the range 500–550 were reported by Li (1954), Sergeev (1966), Hino, Sawamoto & Takasu (1976) and Ohmi *et al.* (1982). The transition to turbulence observed in such studies occurs only during the decelerating phase in the form of violent turbulent bursts, and gives rise to significant modification of the laminar velocity profile.

Perturbations to the laminar Stokes layer have also been observed at lower Reynolds numbers falling in the range 70–550 (Merkli & Thomann 1975; Hino *et al.* 1976; Ohmi *et al.* 1982). In such cases the perturbations do not lead to significant modification of the laminar velocity profile.

Other experimental studies have been performed with the aim of identifying the vortex structures generated after the laminar flow has become unstable. Hayashi & Ohashi (1982) carried out flow visualizations of the Stokes layer and observed the presence of vortex structures, but they did not provide explanations about their origin. Recently, Carstensen, Sumer & Fredsøe (2010) carried out a series of experimental flow visualizations of the Stokes layer in an oscillating water tunnel and emphasized the existence of two different types of coherent vortex structures, referred to as vortex tubes and turbulent spots. Vortex tubes, which are the subject of the present study, are essentially two-dimensional vortices which span the width of the tunnel and emerge when the Reynolds number is in the range 374–776. According to Carstensen *et al.* (2010), vortex tubes are due to an inflection point instability. The turbulent spots appear at R_δ larger than 550 and are three-dimensional vortex structures which emerge within isolated areas, outside of which the flow is laminar.

Several studies have been performed to provide a theoretical framework for the experimental findings relating to the transition in a Stokes layer. Many of these employ linear stability theory to determine the Reynolds number for which the laminar flow becomes unstable. Essentially, two classes of linear stability analysis have been used.

The first class includes analyses based on the assumption of a quasi-steady basic flow, as used in the work of Obremski & Markovin (1969), Tromans (1977) and Monkewitz & Bunster (1987). By using this approach, von Kerczec & Davis (1974) and Blondeaux & Seminara (1979) showed that the flow is unstable for $R_\delta > 85$, near the flow reversal, and that the wavenumber $\alpha = 2\pi\delta^*/l^*$ of the most unstable mode is 0.5. Unfortunately, this kind of analysis has been questioned, since even though it predicts the growth of disturbances at certain phases it does not ensure that disturbances grow or decay during a period of oscillation, because of the assumption that the basic flow is steady.

Linear stability analyses belonging to the second class are based on Floquet theory, which does not introduce a restrictive hypothesis on the basic flow and correctly assumes that the disturbances are periodic in time. The first analyses of this kind were those of von Kerczec & Davis (1974) and Hall (1978), but these failed to detect any linear instability in the flow. Only since the work of Blennerhassett & Bassom (2002) has it become clear that the Stokes layer is unstable for $R_\delta > R_{\delta_c} = 1416$ and that

https://doi.org/10.1017/jfm.2013.274 Published online by Cambridge University Press

the wavenumber α_c of the most unstable mode is $\sim$0.38. However, since this critical Reynolds number is much larger than those at which instability is experimentally detected, Floquet theory does not appear to be capable of explaining the experimental findings either.

The results provided by Floquet theory can be reconciled with those of the experiments by considering the existence of external disturbances that act on the flow (Luo & Wu 2010). In a laboratory experiment exogenous disturbances may arise from different sources, such as vibrations of the facility, spurious effects of the driving mechanism and wall imperfections. Disturbances of this kind act continuously on the flow, so they could excite Floquet modes, by receptivity, even at Reynolds numbers much smaller than $R_{\delta_c} = 1416$, thus making the flow linearly unstable. This fact has been recently demonstrated by Luo & Wu (2010), who simulated the flow by using the linearized Navier–Stokes equations and introducing roughness as a source of disturbances.

In view of the above-mentioned results about the effect of external disturbances, the assertion of Carstensen *et al.* (2010), according to which the inception of the vortex tubes is due to an instability, must be considered to be correct, even though the experiments were carried out at a Reynolds number smaller than $R_{\delta c}$. Therefore, the generation mechanism of these vortices is well understood, and what remains unclear is how these vortices interact with the background vorticity field and among themselves, and how they affect the wall shear stress. The aim of the present study is to improve our insights on these aspects, which were not sufficiently investigated by Carstensen *et al.* (2010) because of experimental constraints. The present investigation does not cover the turbulent spots (Carstensen *et al.* 2010), for which there are currently no studies that explain their generation. However, it seems likely that the mechanism of generation of these structures is linked to that of the transition from laminar to three-dimensional turbulent flow. As reported by Akhavan, Kamm & Shapiro (1991), the transition to turbulence in a Stokes layer can be explained by the interaction between large two-dimensional perturbations with infinitesimal three-dimensional modes. In this regard the vortex tubes may well represent the large two-dimensional perturbations required by this mechanism of transition.

The remaining part of this section is mainly devoted to a review of the literature on the second subject of this paper, i.e. the boundary layer under solitary waves.

Theoretical studies on the boundary layer under solitary waves, and in general under transient long waves, have been carried out by Liu & Orfila (2004). They showed that, while the wave approaches a given position, the velocity increases in the direction of wave propagation, both in the irrotational region and in the boundary layer. During the decelerating phase, the flow in the boundary layer reverses direction, even though in the irrotational region it continues to have the same direction of wave propagation. Liu, Park & Cowen (2007) extended the work of Liu & Orfila (2004), taking into account the nonlinear effects, and concluded that the nonlinearities slightly modify the boundary layer solution even for large waves.

The vortex structures that develop in a solitary wave boundary layer have been studied experimentally by Sumer *et al.* (2010), by using the same experimental facility of Carstensen *et al.* (2010). The authors introduced a Reynolds number Re based on the maximum of the free stream velocity and on half the displacement of fluid particles at the outer edge of the boundary layer. In the present study we use the Reynolds number R_δ, which is related to Re through the expression $R_\delta = \sqrt{2Re}$. Sumer *et al.* (2010) reported that for $R_\delta < 1000$ the flow is laminar with vortex tubes, while for $R_\delta > 1000$ turbulent spots emerge. According to the authors the vortex tubes appear

https://doi.org/10.1017/jfm.2013.274 Published online by Cambridge University Press

during the decelerating phase and are the result of an inflection point shear layer instability, as in the case of the Stokes boundary layer.

Direct numerical simulations of the solitary wave boundary layer have been performed by Vittori & Blondeaux (2008), who showed that the motion can become turbulent after the passage of the wave crest and that the flow reversal is affected by the turbulence.

A linear stability analysis of the bottom boundary layer under solitary waves has recently been carried out by Blondeaux, Pralits & Vittori (2012), who employed a quasi-steady approach. The authors report that the laminar regime becomes unstable during the decelerating phase, when the Reynolds number exceeds a certain value. This is in agreement with the experiments of Sumer *et al.* (2010), who observed vortex tubes during the same phase. Further results of this stability analysis will be recalled in § 4, in conjunction with the discussion of the present results.

The analysis of the vortex tubes under a solitary wave constitutes the second subject of the present paper, with the same aims and motivations previously explained for the Stokes layer. Since the vortex tubes are essentially two-dimensional, we describe them by using the governing equations for a two-dimensional flow, in the vorticity streamfunction formulation, which allows us to perform the present numerical simulations with high efficiency. Wall imperfections of small amplitude are introduced as a source of disturbances (Blondeaux & Vittori 1994); however, from a macroscopic point of view the wall can be regarded as flat. As already pointed out, the turbulent spots are set aside in the present study. This choice is mainly due to the fact that the intrinsic three-dimensionality of the turbulent spots requires the use of a very large three-dimensional computational grid, which does not allow the level of detail of the present numerical simulations to be achieved with reasonable computational costs.

Information on the turbulent spots in the Stokes layer, coming from numerical simulations, can be found in Mazzuoli, Vittori & Blondeaux (2011).

The paper is organized as follows. In § 2 the problem is formulated and the adopted numerical approach described. In § 3 and in § 4, results are presented for vortex structures under progressive and solitary waves, respectively. In § 5 conclusions are drawn.

2. The governing equations and the numerical approach

We consider the bottom boundary layer of both progressive and solitary waves on a wall characterized by imperfections of small amplitude. At the outer edge of the bottom boundary layer of progressive waves, the fluid oscillates as $u^* = u_0^* \sin(\sigma^* t^*)$, where u_0^* is the amplitude of the velocity oscillations, σ^* is the angular frequency and t^* is the time. In the case of a solitary wave, we follow Sumer *et al.* (2010) and assume that at the outer edge of the bottom boundary layer the velocity varies as $u^* = u_0^* \,\mathrm{sech}^2(\sigma^* t^* - \pi)$. The quantity $T^* = 2\pi/\sigma^*$ is defined as the temporal extension of the solitary wave. The term π in the expression of u^* is introduced here in order to have the maximum of u^* at $t^* = T^*/2$.

As a reference, a Cartesian coordinate system with the x^* axis lying on the bottom and the y^* axis pointing upwards is employed. The problem is formulated in dimensionless form, in terms of vorticity and streamfunction, by introducing the dimensionless variables

$$t = t^*\sigma^*, \quad (x, y) = \frac{(x^*, y^*)}{\delta^*}, \quad (u, v) = \frac{(u^*, v^*)}{u_0^*}, \quad \psi = \frac{\psi^*}{u_0^*\delta^*}, \quad \omega = \frac{\omega^*\delta^*}{u_0^*}, \quad (2.1)$$

https://doi.org/10.1017/jfm.2013.274 Published online by Cambridge University Press

where (u^*, v^*) are the velocity components, ψ^* is the streamfunction and ω^* is the vorticity. The conventional thickness of the boundary layer δ^* is given by $\sqrt{2\nu^*/\sigma^*}$ for both types of wave. We also introduce the wall shear stress τ_0^*, which is the component of the stress tangent to the wall, defined in dimensionless form as $\tau_0 = \tau_0^*/\varrho u_0^{*2}$.

The wall is characterized by imperfections having a spatial periodicity L_ξ and described by

$$x = \xi - \sum_{n=1}^{N} \frac{h_n}{2} \sin(n\alpha\xi + \phi_n), \quad y = \sum_{n=1}^{N} \frac{h_n}{2} \cos(n\alpha\xi + \phi_n), \tag{2.2}$$

where ξ is a dummy variable ranging from 0 to L_ξ and $\alpha = 2\pi/L_\xi$ is the wavenumber. The governing equations are written in an orthogonal curvilinear coordinate system (ξ, η) described by

$$x = \xi - \sum_{n=1}^{N} \frac{h_n}{2} \mathrm{e}^{-n\alpha\eta} \sin(n\alpha\xi + \phi_n), \quad y = \eta + \sum_{n=1}^{N} \frac{h_n}{2} \mathrm{e}^{-n\alpha\eta} \cos(n\alpha\xi + \phi_n), \tag{2.3}$$

where the wall profile (2.2) is recovered by setting $\eta = 0$ in (2.3). The velocity components having the direction of these coordinates are denoted by (u_ξ, u_η). The vorticity equation and the equation that links the vorticity to the streamfunction, in the curvilinear coordinate system described by (2.3), in dimensionless form read

$$\frac{\partial \omega}{\partial t} + \frac{R_\delta}{2J} \left(\frac{\partial \psi}{\partial \eta} \frac{\partial \omega}{\partial \xi} - \frac{\partial \psi}{\partial \xi} \frac{\partial \omega}{\partial \eta} \right) = \frac{1}{2J} \left(\frac{\partial^2 \omega}{\partial \xi^2} + \frac{\partial^2 \omega}{\partial \eta^2} \right), \tag{2.4}$$

$$\frac{1}{J} \left(\frac{\partial^2 \psi}{\partial^2 \xi} + \frac{\partial^2 \psi}{\partial^2 \eta} \right) = -\omega, \tag{2.5}$$

where J is the Jacobian of the coordinate transformation. These equations have been integrated in a rectangular domain of dimensions L_ξ and L_η along the ξ and η directions respectively. On the wall ($\eta = 0$), the no-slip boundary condition has been introduced along with the vanishing of the streamfunction,

$$\left(\frac{\partial \psi}{\partial \eta}, \psi \right) = (0, 0) \quad \text{at } \eta = 0, \tag{2.6}$$

while periodic boundary conditions have been introduced along the ξ direction. The vorticity on the no-slip wall has been computed according to the method proposed by Thom (1928). Finally, far from the wall, the condition which forces the fluid to move as $u = \sin(t)$ or as $u = \mathrm{sech}^2(t - \pi)$ has been introduced for a progressive and a solitary wave respectively. After the value of L_η has been fixed large enough, such that at $\eta = L_\eta$ negligible values of vorticity are present, the above conditions have been introduced by imposing $(1/\sqrt{J})\partial\psi/\partial\eta = u$ at $\eta = L_\eta$.

The numerical approach uses centred second-order finite differences for the spatial derivatives on a grid made up of n_ξ and n_η nodes along the ξ and the η directions respectively. The grid is uniform in the ξ direction and stretched in the η direction in order to cluster the grid points close to the wall where the gradients are large. The stretching is obtained by the hyperbolic tangent function. The time advancement has been carried out by the Crank–Nicolson scheme for the diffusive term and by a third-order Runge–Kutta scheme for the convective term. With regard to the spatial discretization, the convective term has been computed according to the second-order

https://doi.org/10.1017/jfm.2013.274 Published online by Cambridge University Press

numerical scheme proposed by Arakawa (1966), which allows the kinetic energy and the enstrophy to be conserved in the absence of viscous dissipations and time-discretization errors.

To check the correctness of the numerical code, we computed the vorticity field on a wavy wall characterized by $N = 1$, $h_1 = 5$ and $L_\xi = 33.325$ for $R_\delta = 50$, and compared the results with those shown in figure 3 of Scandura, Vittori & Blondeaux (2000), where such flow has been computed by solving the governing equations in the primitive variables formulation. The comparison showed good agreement between the two results. In this computation we fixed $L_\eta = 33.325$, $n_\xi = 120$ and $n_\eta = 120$, of which 12 points were clustered within a distance δ from the wall.

3. Vortex structures in the boundary layer under progressive waves

Before studying the vortex structures we analyse how the flow responds when disturbed by wall imperfections of sinusoidal shape of small amplitude. The wall is described by (2.2), where we set $N = 1$ and $\phi_1 = 0$. Hence, the flow is characterized by three dimensionless parameters: R_δ, h_1/L_ξ and α. We consider the flow response as a function of α for three Reynolds numbers, $R_\delta = 763$, 600 and 50 and h_1/L_ξ fixed at 1.2×10^{-4}. One can easily check that for $h_1/L_\xi \ll 1$ (2.2) is very close to a sine wave. The governing equations are solved by using a numerical grid with n_ξ ranging from 200 to 300, the exact value being dependent on L_ξ, and $n_\eta = 440$. About 70 of the 440 grid points are clustered inside the thickness of the boundary layer δ. It has been ensured that a further refinement of the grid does not affect the results. The dimension L_η is fixed at 40 in all calculations because it has been found that such a value is largely sufficient to avoid interactions of the vortex structures with the upper boundary of the computational domain, which could negatively affect the results. Finally, a time step no larger than 2×10^{-4} is employed.

We emphasize that a drawback arises in quantifying the global destabilizing effect of the wall imperfections, since a basic flow against which to assess the deviations of the actual flow is not definable in the case of a wavy wall. With the purpose of solving this problem, we observe that when the flow is stable and the boundary layer stays attached to the wall, the velocity component u_η along the η direction is very small, as the η coordinate is orthogonal to the wall. On the other hand, when the boundary layer is unstable, the velocity u_η becomes relatively large, because of the appearance of vortices. Hence, as a measure of the destabilizing effect of the wall imperfections we use the maximum absolute value $|u_\eta|_{max}$ of the velocity component having the direction of the η coordinate.

In figure 1(*a–c*) the trend of $|u_\eta|_{max}$ versus α for $R_\delta = 762$, 600 and 50, respectively, is shown for the case of a wall affected by sinusoidal imperfections. It is worthwhile pointing out that the position in space of $|u_\eta|_{max}$ is not fixed but depends on the flow parameters.

We observe that the largest flow response is attained for $\alpha \approx 0.36$ in figure 1(*a*) and for $\alpha \approx 0.35$ in figure 1(*b*). It is interesting that such wavenumbers are very close to that of the most unstable mode predicted by Floquet linear stability theory ($\alpha_c = 0.38$; Blennerhassett & Bassom 2002), even though the present Reynolds numbers are significantly smaller than $R_{\delta_c} = 1416$ and all the flow nonlinearities have been retained in the governing equations. Figure 1(*c*) shows that when the Reynolds number is equal to 50, the flow response decreases substantially and the maximum is attained for wavenumbers significantly smaller than α_c.

https://doi.org/10.1017/jfm.2013.274 Published online by Cambridge University Press

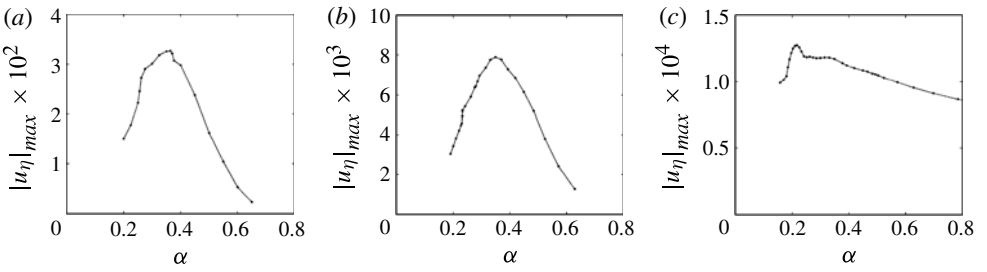


FIGURE 1. Boundary layer under progressive waves. Maximum absolute value $|u_\eta|_{max}$ of the velocity component along the η coordinate versus the wavenumber $\alpha = 2\pi/L_\xi$ of sinusoidal wall perturbations, for $h_1/L_\xi = 1.2 \times 10^{-4}$: (*a*) $R_\delta = 762$, (*b*) $R_\delta = 600$, (*c*) $R_\delta = 50$.

Although $|u_\eta|_{max}$ is much smaller than 1, it is rather large when compared with the slope of the wall ($h_1/L_\xi = 1.2 \times 10^{-4}$). For example, with reference to figure 1(*a*), the ratio between the peak of $|u_\eta|_{max}$ and the slope is ∼260. Hence, wall imperfections, even of small amplitude, are able to trigger flow perturbations of relatively large amplitude, thus supporting the hypothesis that the two-dimensional instability detected experimentally, at subcritical Reynolds numbers (Carstensen *et al.* 2010), is due to external disturbances.

The present findings are in qualitative agreement with those of Luo & Wu (2010), but, from a quantitative point of view, the flow response obtained by the previous authors is larger than the present one, probably because of the absence of nonlinear effects in their simulations. Finally, we observe that if the wall imperfections are removed, the disturbances disappear and the flow turns out to be one-dimensional, except in the case in which the Reynolds number is greater than 1416. In the last case the disturbances are self-sustaining from one cycle to another, in agreement with Floquet linear stability theory.

After this preliminary analysis we come to the core of the present investigation, whose task is to reproduce numerically and analyse the vortex structures observed experimentally by Carstensen *et al.* (2010). In order to display the vortices that develop in the Stokes layer, Carstensen *et al.* (2010) released a thin layer of diluted skimmed milk on the bottom of an oscillating water tunnel, while the fluid was at rest. Then the amplitude of oscillation was increased steadily and at the same time the flow was videotaped and the bed shear stress sampled. We focus on test 7, for which results in figures 7 and 8 of Carstensen *et al.* (2010) are shown during the third half-cycle. The Reynolds number Re, based on the amplitude of fluid oscillations at the outer edge of the boundary layer, was 3.0×10^5 during the third half-cycle, which corresponds to $R_\delta = \sqrt{2Re} = 775$.

In order to reproduce this experiment as closely as possible, the numerical simulation is performed starting with the fluid at rest and increasing the amplitude of the velocity oscillations linearly in time to get $R_\delta = 775$ in the third half-cycle. Moreover, wall imperfections similar to those of a real wall are introduced by using (2.2), where N is set equal to 80 and h_n and ϕ_n are randomly generated. From a statistical point of view, h_n and ϕ_n are uniformly distributed in the ranges 0–0.005 and 0–2π respectively. After fixing $L_\xi = 64\pi$, the wall thus generated is shown in figure 2. It is appropriate to provide a dimensional value of the amplitude of the wall imperfections in figure 2 that emphasizes how big they are. The peak of the wall imperfections is ∼0.028 at $x \approx 120$. By assuming for δ^* the value of the experiments

https://doi.org/10.1017/jfm.2013.274 Published online by Cambridge University Press

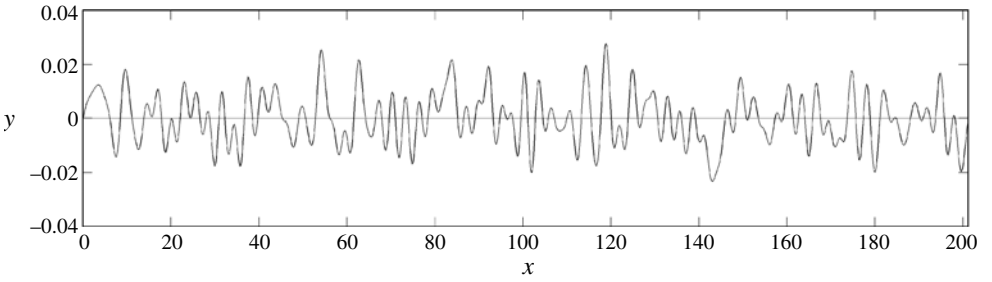


FIGURE 2. Profile of the wall used to compute the flow in the boundary layer under both progressive and solitary waves.

of Carstensen *et al.* (2010), which is equal to 1.7×10^{-3} m, the peak takes the value $0.028\delta^* = 4.76 \times 10^{-5}$ m.

The dimension L_η is fixed at 40 as in the previous simulations and the computational grid is characterized by $n_\xi = 3000$ and $n_\eta = 440$, of which 70 are clustered inside the thickness of the boundary layer δ, as in the previous simulations. The grid resolution in the ξ direction is sufficient to capture the highest wavenumber components of the wall. Indeed, the shortest wavelength is described by $n_\xi/N = 37$ grid points, where $N = 80$ is the number of Fourier components of the wall imperfections. Moreover, we carried out several simulations by using 1500 grid points in the ξ direction, and in all cases the results were almost indistinguishable from those obtained by setting $n_\xi = 3000$.

A layer of tracers, of thickness $1.58\delta^*$, is released close to the bed at the beginning of the simulation. The subsequent motion of the tracers is computed by using a Lagrangian particle tracker, with the aim of visualizing the flow. This numerical flow visualization technique mimics that of Carstensen *et al.* (2010) and allows a more exhaustive comparison between experimental and numerical results.

In figure 3, where the vorticity contours, the mean velocity profiles and the wall shear stresses are shown at different phases, the presence of an inflection point in the velocity profile is the reason for the instability of the vortex layer, characterized by negative vorticity, which leads to the appearance of several vortices. The instability mechanism can be explained physically as follows (Drazin & Reid 2004). Let us consider a sinusoidal perturbation of the vortex layer sufficiently small to make appropriate a linearization of the governing equations. The linearized vorticity equation shows that at the inflection point ($y = y_i$) the perturbed vorticity is mainly advected by the basic flow, as $\partial\langle\omega\rangle/\partial y = 0$, where $\langle\omega\rangle$ is the vorticity of the basic flow. In a reference system moving with the velocity of the basic flow at the inflection point, for $y > y_i$ the velocity is positive while for $y < y_i$ it is negative. Therefore, crests and troughs of the perturbation travel in opposite directions. This causes steepening of the sinusoidal perturbation and the concentration of vorticity in the zero-down crossing positions of the waviness. The concentration of vorticity induces a swirling motion of fluid particles that can be more clearly observed in figure 5(*d*), where the distribution of tracers released at the beginning of the simulation is shown. Therefore, vortices are generated which correspond to those denoted by Carstensen *et al.* (2010) as vortex tubes.

The onset of this instability is near the flow reversal, indeed at $\phi = 178.6°$ several vortices emerge at the inflection point of the velocity profile in figure 3(*a*). The first issue we discuss concerns the determination of the average distance between two

https://doi.org/10.1017/jfm.2013.274 Published online by Cambridge University Press

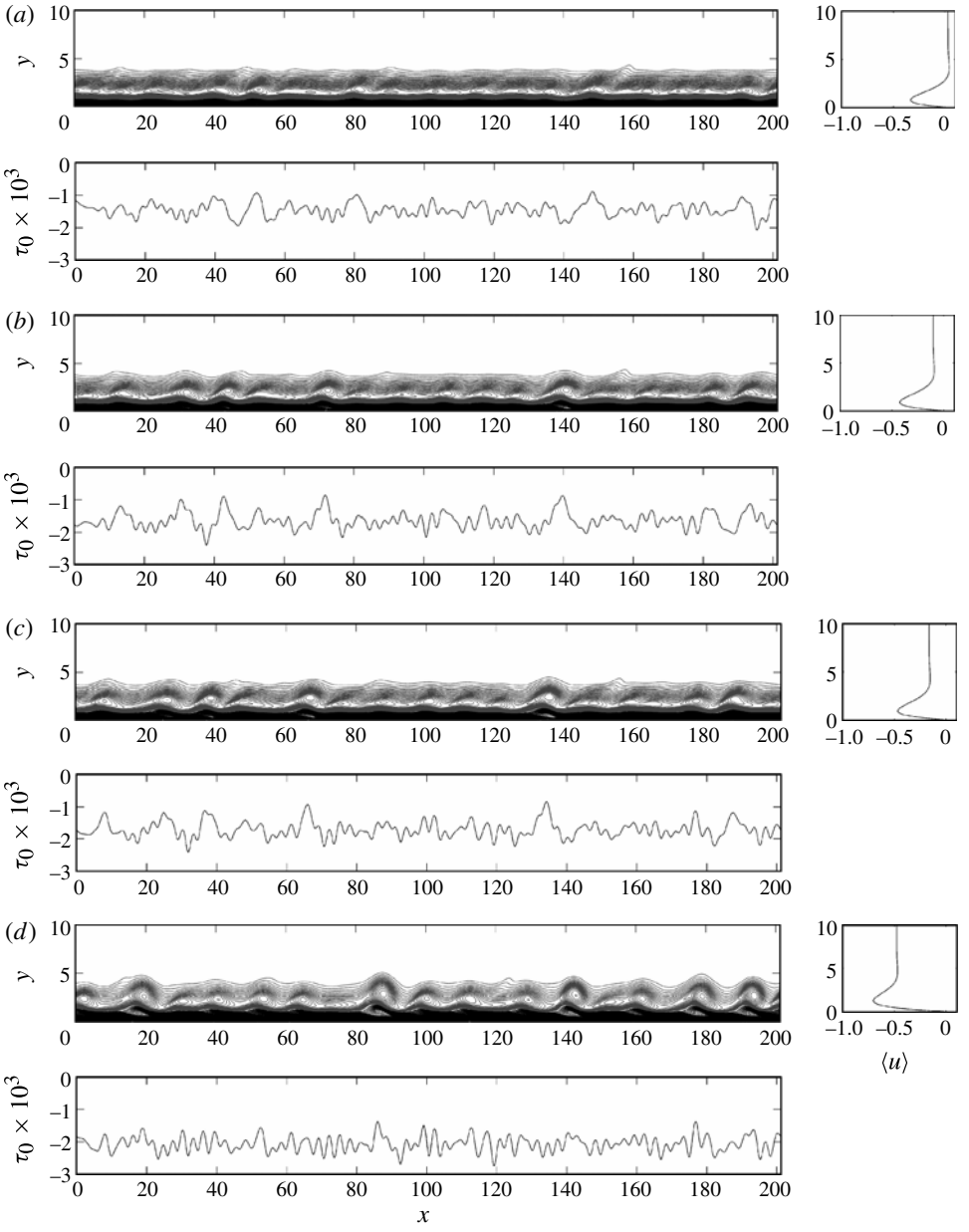


FIGURE 3. Vorticity contours, mean velocity profiles and wall shear stress τ_0 at different phases near the end of the third half-cycle, for a flow in which the amplitude of oscillation increases steadily with time, for $R_\delta = 775$ (test 7 of Carstensen *et al.* 2010): (*a*) $t = 9.40$, $\phi = 178.6°$; (*b*) $t = 9.51$, $\phi = 184.9°$; (*c*) $t = 9.56$, $\phi = 187.7°$; (*d*) $t = 9.82$, $\phi = 202.64°$. Black lines, $\omega > 0$, $\Delta\omega = 0.03$; grey lines, $\omega < 0$, $\Delta\omega = 0.01$.

vortex tubes, defined as the ratio between the length of the computational domain L_ξ and the number of vortices. Since in figure 3 phases are displayed in which the vortices are very weak and not well defined, the mean spacing appears to be rather elusive to quantify. Therefore, in order to determine the number of vortices as

https://doi.org/10.1017/jfm.2013.274 Published online by Cambridge University Press

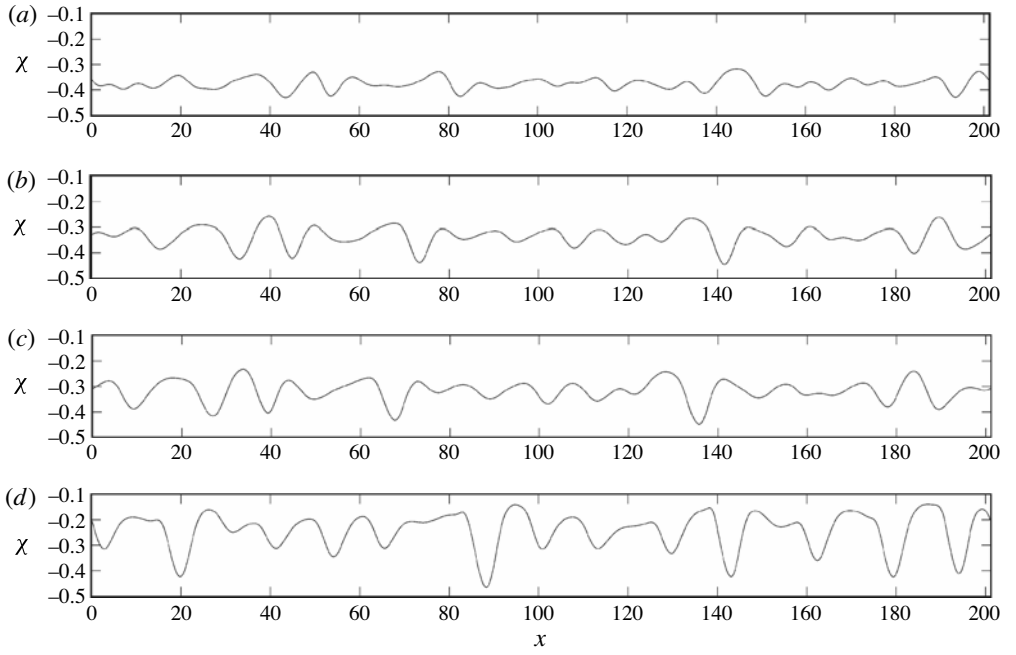


FIGURE 4. Distribution of the function χ, for $R_\delta = 775$: (*a*) $t = 9.40$, $\phi = 178.6°$; (*b*) $t = 9.51$, $\phi = 184.9°$; (*c*) $t = 9.56$, $\phi = 187.7°$; (*d*) $t = 9.82$, $\phi = 202.64°$.

objectively as possible, the following function is introduced:

$$\chi(x) = \int_0^{L_\eta} \omega^- \, \mathrm{d}y, \tag{3.1}$$

where $\omega^- = \omega$ if $\omega < 0$ and $\omega^- = 0$ otherwise. The function χ exhibits a minimum where the negative vorticity concentrates to form a vortex tube. By counting the number of minima of χ, we obtain the number of negative vortices in the flow at a certain time. In figure 4 the trend of the function χ is shown at the same phases shown in figure 3. The number of vortices N_v and the mean spacing ℓ_m at the phases (*a–d*) are (*a*) $N_v = 19$, $\ell_m = 10.58$, (*b*) $N_v = 17$, $\ell_m = 11.82$, (*c,d*) $N_v = 16$, $\ell_m = 4\pi$. We observe a decrease of N_v during the flow development, which is due to the phenomenon of merging between pairs of vortex tubes. This phenomenon will be better illustrated in the following.

Let us now determine the number of vortices by using figure 5, where the distribution of tracers is shown at the same phases of figure 3. This figure provides a more faithful reproduction, compared to figure 3, of the vortex tubes observed experimentally by Carstensen *et al.* (2010). We observe that as the flow develops, the layer of tracers is lifted up at certain locations and finally vortex tubes emerge. Overall, 14 vortex tubes can be detected at $\phi = 202.64°$ (figure 5*d*). Hence, the average spacing between two adjacent vortices is 14.36, which is very close to the value reported by Carstensen *et al.* (2010). By carefully analysing figure 5(*d*), the imprint of two additional vortices can be observed at $x \approx 70$ and $x \approx 150$, in agreement with figure 3(*d*), where 16 vortices are detected. However, the two additional vortices

https://doi.org/10.1017/jfm.2013.274 Published online by Cambridge University Press

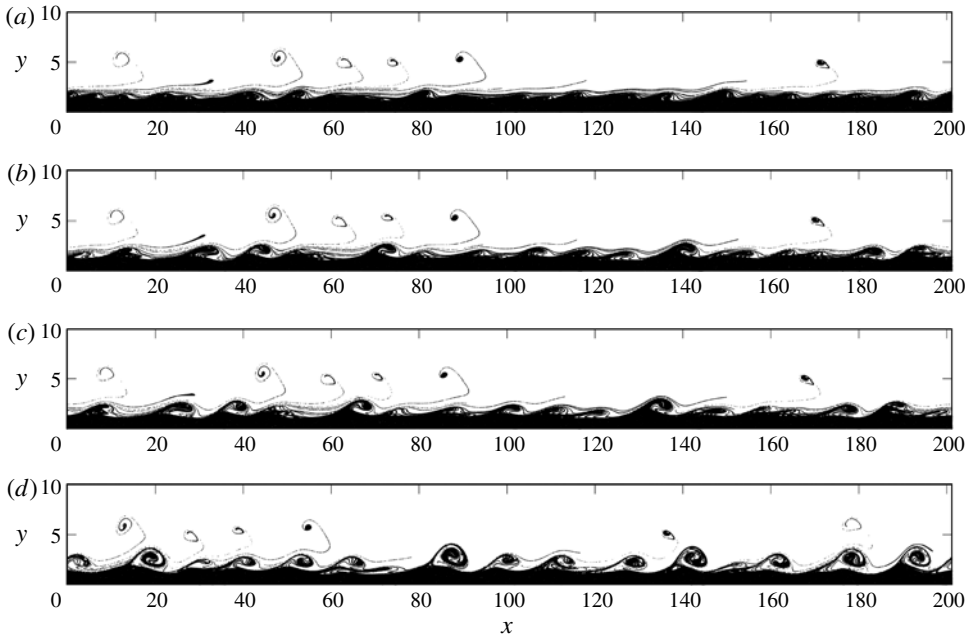


FIGURE 5. Distribution of tracers released at the beginning of the simulation in a boundary layer in which the amplitude of oscillation increases steadily with time, for $R_\delta = 775$ (test 7 of Carstensen *et al.* 2010): (*a*) $t = 9.40, \phi = 178.6°$, (*b*) $t = 9.51, \phi = 184.9°$ (*c*) $t = 9.56, \phi = 187.7°$ (*d*) $t = 9.82, \phi = 202.64°$.

are very weak and probably could not be displayed in a physical experiment. Therefore, with confidence, the present results can be considered consistent with those of Carstensen *et al.* (2010).

Figure 3(*d*) shows that the positive vortex layer adjacent to the wall becomes wavy. In the fourth half-cycle (figure 6) the vortex layer rolls up, generating several positive vortices. The destabilization of this vortex layer follows a path that bypasses the linear instability mechanism described for the negative vortex layer, from which the vortex tubes originate.

We describe the destabilization of the positive vortex layer with the help of figure 7, where the vorticity and pressure fields generated by a specific vortex structure is shown at four different phases. This vortex structure can be detected in figure 3(*d*), by using as a reference the range of x shown in figure 7(*a*). The pressure is determined by solving the Poisson equation, derived by taking the divergence of the Navier–Stokes equations.

In figure 7(*a*) we observe that the vortex tube generates a region of low pressure in which the minimum is located in the centroid of the vortex tube itself. The low pressure is felt throughout the positive vortex layer up to the wall, where it induces a favourable pressure gradient ($\partial p/\partial x > 0$) for $87.5 < x < 92$ and an adverse pressure gradient ($\partial p/\partial x < 0$) for $80 < x < 87.5$ (the flow is directed from right to left). The adverse pressure gradient causes a localized decrease in the u velocity component. Therefore, because of mass conservation, the v velocity component increases, giving rise to a hump in the positive vortex layer. The decrease in the u velocity component is not uniform across the layer and this produces a folding of the positive vorticity

https://doi.org/10.1017/jfm.2013.274 Published online by Cambridge University Press

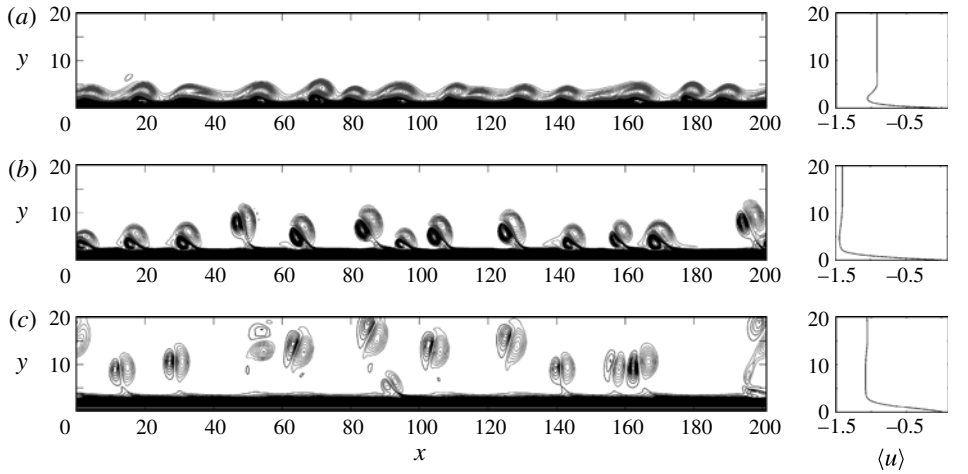


FIGURE 6. Vorticity contours and mean velocity profiles at different phases during the fourth half-cycle for a flow in which the amplitude of fluid oscillations increases steadily with time for $R_\delta = 775$ (test 7 of Carstensen *et al.* 2010): (*a*) $t = 10.21$, $\phi = 225°$; (*b*) $t = 11.00$, $\phi = 270°$; (*c*) $t = 11.78$, $\phi = 315°$. Black lines, $\omega > 0$; grey lines, $\omega < 0$; $\Delta\omega = 0.01$.

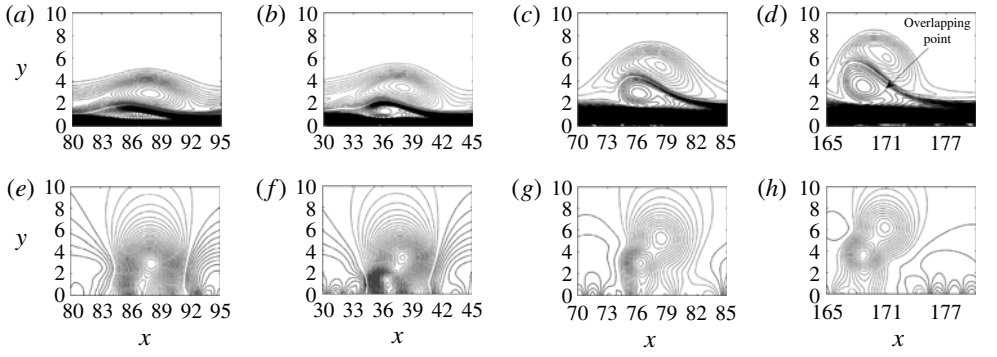


FIGURE 7. Vorticity contours (*a–d*) and pressure contours (*e–h*) pertinent to a vortex structure which occupies different positions as the flow develops: (*a,e*) $t = 9.82$, (*b,f*) $t = 10.00$, (*c,g*) $t = 10.80$, (*d,h*) $t = 11.00$. Black lines, $(\omega, p) > 0$; grey lines, $(\omega, p) < 0$; $\Delta\omega = 0.02$ for $\omega > 0$, $\Delta\omega = 0.01$ for $\omega < 0$; $\Delta p = 5 \times 10^{-4}$.

isolines as shown in figure 7(*a*). Moreover, the vorticity-induced velocity gives rise to an anticlockwise swirling motion of fluid particles which enhances the folding. Therefore, it happens that two points belonging to the same vorticity isoline overlap, generating a closed loop. This is shown in figure 7(*b–d*). In particular, the arrow in figure 7(*d*) shows the approximate location where this overlap occurs. The accumulation of closed loops indicates that an anticlockwise vortex has been formed, as confirmed by the appearance of another minimum in the pressure distribution shown in figure 7(*f–h*). This new vortex and the vortex tube form a pair of counter-rotating vortices which leave the bottom because of the self-induced velocity. This is therefore the mechanism that causes the movement of the vortices away from the wall. The presence of vortex pairs was not detected in the experiments of Carstensen *et al.* (2010).

https://doi.org/10.1017/jfm.2013.274 Published online by Cambridge University Press

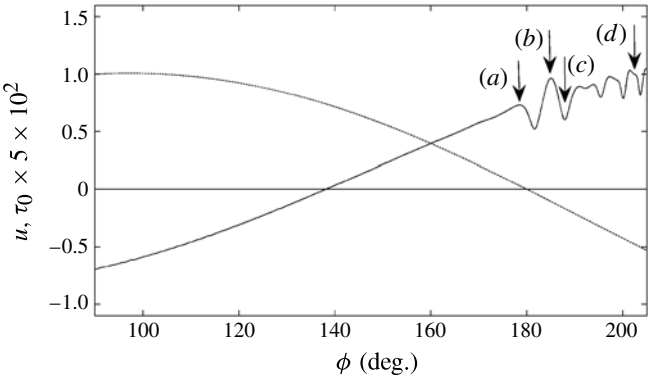


FIGURE 8. Time development of the velocity u in the irrotational region (dashed line) and of the dimensionless wall shear stress $\tau_0 = \tau_0^*/(\varrho u_0^{*2})$ (continuous line) at $x = 187.6$, during the third half-cycle, for $R_\delta = 775$ (test 7 of Carstensen *et al.* 2010). The sign of τ_0 is reversed with respect to that in figure 3. The phases (*a–d*), shown by arrows, correspond to the phases of figure 3(*a–d*) respectively.

The destabilization of the positive vortex layer has implications for the wall shear stress. In figure 3, several humps in the positive vortex layer adjacent to the wall can be observed which are generated as previously described. Where the thickness of the vortex layer increases (decreases), the velocity gradient close to the wall decreases (increases), and therefore a decrease (increase) of the wall shear stress is detected. For instance, in figure 3(*b*), at $x \approx 140$, we observe a thickening of the positive vortex layer which is accompanied by a decrease in the wall shear stress in absolute terms. Since the vortex tubes move along the x direction approximately with the velocity of the basic flow at the inflection point of the velocity profile, high-frequency fluctuations of the wall shear stress are detected at a fixed location. Indeed, in figure 8, where the time development of the velocity in the irrotational region and of the wall shear stress τ_0 at $x = 187.6$ are shown, when the vortex tubes start to appear, at about $\phi = 180°$, high-frequency fluctuations of the wall stress are generated.

We emphasize that in figure 8 the sign of the wall shear stress has been reversed to facilitate comparison with figure 8 of Carstensen *et al.* (2010). We can see that the qualitative agreement between the two figures is fairly good. The arrows in figure 8 indicate the phases of figure 3(*a–d*), and are shown to make it easier to check that the fluctuations of τ_0 are consistent with the mechanism described above. When the flow develops further, the vortex tubes move away from the wall and the amplitude of the wall shear stress fluctuations gradually decays to low values.

While the processes described above are taking place, the vortex merging phenomenon, already mentioned, continues to operate, causing a further decrease in the number of vortices. Indeed, in figure 6(*a–c*) we observe 15, 13 and 12 vortices respectively. The loss of two vortices when passing from figures 6(*a*) to 6(*b*) is due to the two vortices located in $105 < x < 125$ in figure 6(*a*), which coalesce in the vortex located in $x \approx 130$ in figure 6(*b*), and to the two vortices located in $148 < x < 170$ in figure 6(*a*), which coalesce in the vortex located at $x \approx 170$ in figure 6(*b*). This shows that vortex merging is an important phenomenon that affects the mean spacing between the vortices.

At this stage we have enough information to perform a comparison of the phases of inception and disappearance of the vortex tubes with those observed by

https://doi.org/10.1017/jfm.2013.274 Published online by Cambridge University Press

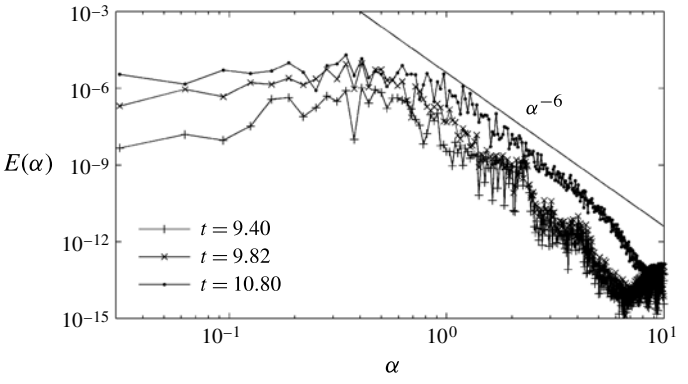


FIGURE 9. Spectra of the kinetic energy of the boundary layer under progressive waves at different phases: $R_\delta = 775$.

Carstensen *et al.* (2010). The authors reported that the inception and disappearance of the vortex tubes fall in the ranges 150–175° and 200–245° respectively, with negligible dependence on the Reynolds number. In the present study the phase of inception falls in the range 170–175°, which belongs to the upper part of the range indicated by Carstensen *et al.* (2010). On the other hand, the present results disagree significantly with those of Carstensen *et al.* (2010) with regard to the phases of disappearance. Indeed, at $\phi = 270°$ in figure 6(*b*) we still observe vortex tubes, while according to Carstensen *et al.* (2010) they do not survive beyond $\phi = 245°$. A possible explanation for this discrepancy is that, in the experiments, far from the wall the concentration of dye was not sufficient to display any vortex structure beyond $\phi = 245°$. This could also explain why Carstensen *et al.* (2010) did not mention the existence of vortex pairs.

In these simulations the dissipation of the vortex tubes appears to be a process that decays gradually, over a long time. Therefore the definition of a phase of complete disappearance of the vortices is not particularly meaningful.

Before closing this section we discuss the longitudinal kinetic energy spectra, which provide additional insights into the structure of the flow. Since the flow is periodic only in the streamwise direction, we consider the spatial Fourier transform in the x direction averaged along the y direction,

$$E(\alpha) = \frac{1}{(y_2 - y_1)} \int_{y_1}^{y_2} (|\hat{u}(\alpha, y)|^2 + |\hat{v}(\alpha, y)|^2)\, \mathrm{d}y, \tag{3.2}$$

where $\hat{u}$ and $\hat{v}$ are the Fourier transform of u and v, $(y_2 - y_1)$ is the y range over which the average is computed, and α is the wavenumber, in the present context defined as $\alpha = n2\pi/L_\xi$. Since the velocities are known in a curvilinear coordinate system, before performing the transformation in the x direction, the velocity is interpolated on a Cartesian grid made up of the same number of points as the curvilinear grid. The coordinate y_1 is fixed at 2.94×10^{-2}, which is just above the peak of the wall perturbation, while y_2 is equal to $L_\eta = 40$. Before discussing the spectra shown in figure 9, we recall that the instability of the present flow is due to unstable waves induced by the wall imperfections.

Therefore, it is expected that near the time of the instability inception ($t \approx 9.34$), the kinetic energy spectra are affected by the spectrum of the wall imperfections. We

https://doi.org/10.1017/jfm.2013.274 Published online by Cambridge University Press

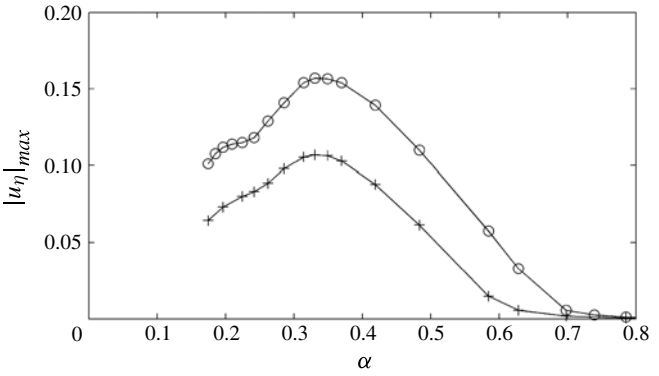


FIGURE 10. Boundary layer under solitary waves. Maximum absolute value $|u_\eta|_{max}$ of the velocity component along the η coordinate versus the wavenumber $\alpha = 2\pi/L_\xi$ of sinusoidal wall perturbations, for $h_1/L_\xi = 1.2 \times 10^{-4}$. Crosses, $R_\delta = 600$; circles, $R_\delta = 762$.

make this clarification to explain, from the outset, that in figure 9 the low value of the twelfth component ($\alpha = 0.375$), at $t = 9.40$, occurs because the random generation of the spectrum of the wall imperfections produced a twelfth component which is an order of magnitude smaller than the neighbours. With time, nonlinear effects cause the spread of energy over a wide range of wavenumbers, so the twelfth component tends to become similar to the others. The peak of the spectra is at $\alpha \approx 0.35$ at all times, in agreement with figure 1(*a*), where the maximum flow response to sinusoidal wall imperfections is obtained for $\alpha \approx 0.36$. At low wavenumbers the components of the spectrum increase with time thanks to the inverse energy cascade that generally characterizes two-dimensional flows. At large wavenumbers the spectrum is very steep, as shown by the α^{-6} power law plotted in figure 9. The steepness is therefore much larger than that due to the α^{-3} power law predicted for both forced and decaying two-dimensional turbulence by Kraichnan (1967) and Batchelor (1969), on the basis of an enstrophy cascade towards large wavenumbers. However, spectra much steeper than α^{-3} have been observed even in other studies. For example, Lesieur *et al.* (1987) found an α^{-4} spectrum in a temporal mixing layer and Bracco *et al.* (2000) reported spectra close to α^{-5} in a decaying two-dimensional turbulence. As reported by Lesieur *et al.* (1987), the enstrophy cascade is due to the shearing by large vortices of small eddies which are elongated in the flow direction and compressed in the transverse direction, which thus become similar to vortex sheets. Since in a two-dimensional flow the vorticity is conserved (the effect of viscosity can be considered small), the formation of the vortex sheets corresponds to a cascade of vorticity to small scales. This explains why flows dominated by coherent vortices, without small-scale vorticity, usually exhibit spectra much steeper than α^{-3} at large wavenumbers. In figures 3 and 6 it can be observed that the flow is dominated by large vortices that survive for a long time. Therefore, very steep energy spectra are fully justified at large wavenumbers.

4. Vortex structures in the boundary layer under solitary waves

As in § 3, we briefly analyse the flow response to wall imperfections of sinusoidal shape. The parameters of the simulations are equal to those used in § 3 and the results are shown in figure 10 for $R_\delta = 762$ and 600. We note that $|u_\eta|_{max}$ decays for both large and small α and reaches a peak for $\alpha \approx 0.34$. This wavenumber is close to

https://doi.org/10.1017/jfm.2013.274 Published online by Cambridge University Press

that of the most unstable Fourier mode predicted by the linear stability analysis of Blondeaux *et al.* (2012), as shown below. In this analysis the lengths are scaled by the thickness δ_B^*, which is related to δ^* by the equation $\delta^* = \delta_B^*(4h^*/(3H^*))^{(1/4)}$, where h^* is the water depth and H^* is the height of the solitary wave above the still water level. There is also a difference in the definition of the phases, which are linked by the relation $\zeta = \zeta_B(3H^*/(4h^*))^{(1/2)} + \pi$. Finally, the present Reynolds number can be expressed as $R_\delta = (2H^*/\delta_B^*)(4h^*/(3H^*))^{(1/4)}$.

For the set of parameters $H^*/h^* = 0.12$ and $\delta_B^*/h^* = 5 \times 10^{-4}$ ($R_\delta = 876$), Blondeaux *et al.* (2012) found that the wavenumber first destabilized is $\alpha_{Bc} = 0.2$, with a very weak variability in the range of Reynolds numbers considered here. Rescaling this wavenumber according to the present rules, by using the previous relations, we obtain $\alpha_c = 0.36$, which is fairly close to the wavenumber that in figure 10 provides the maximum flow response to sinusoidal wall perturbations.

Comparing figure 1 with 10, we observe that under solitary waves wall imperfections are able to trigger flow perturbations that are larger than those under progressive waves, of about five times for $R_\delta = 762$ and 12 times for $R_\delta = 600$.

The next goal is to reproduce numerically the experiments of Sumer *et al.* (2010), with the purpose of gaining new insights into the vortex tubes under solitary waves. To get results consistent with reality, the length L_ξ of the computational domain must be large enough to enable the development of several vortex tubes interacting among themselves. The experiments of Sumer *et al.* (2010) are a guide to deciding whether a value of L_ξ might be adequate. In figure 8 of Sumer *et al.* (2010), where several vortex tubes are displayed, the image covers a width of $\sim$0.28 m. Since in the experiments $T^* = 9.2$ s, the thickness of the boundary layer δ^* is 1.71×10^{-3} m, and hence the image covers a width of $\sim 164\delta^*$. This shows that the wall shown in figure 2 might be adequate, as L_ξ is equal to $64\pi = 201.06$.

The Reynolds number R_δ has been fixed at 748, which is equal to that of figure 8 of Sumer *et al.* (2010). The dimension L_η of the computational domain and the numerical grid are the same as those used in § 3.

In agreement with both the experiments and linear stability theory, the numerical simulations show that the boundary layer is stable during the accelerating phase, while it turns out to be unstable during the decelerating phase. Therefore, the vorticity, the mean velocity profiles and the wall shear stresses are shown in figure 11 at three different instants pertinent to the decelerating phase. As in § 3, it is once again the presence of an inflection point in the velocity profile that causes the instability of the negative vortex layer and the generation of vortex tubes. These vortices, in turn, induce the roll-up of the vortex layer adjacent to the wall (figure 11*a*), characterized by positive vorticity, through the same mechanism described in § 3. The positive vortices thus generated, together with the vortex tubes, form pairs of counter-rotating vortices which move away from the wall (figure 11*c*). Sumer *et al.* (2010) did not mention the formation of vortex pairs, which are in fact difficult to infer from the video frames taken during the experiments. However, after obtaining a better understanding of the processes that take place in the boundary layer, it becomes possible to discern the existence of vortex pairs from the movies therein (Sumer *et al.* 2010, available at http://dx.doi.org/10.1017/S0022112009992837). We consider movie 2 of Sumer *et al.* (2010), during the first 28 frames the flow is unidirectional, from left to right. In frame 36, vortex tubes, characterized by negative vorticity, begin to appear away from the wall, where the dye concentration is rather low. As the vortex tubes grow, they perturb the layer close to the wall, where the dye concentration is large. Within this layer the vorticity is positive, at least in the region closest to the wall. Starting from

https://doi.org/10.1017/jfm.2013.274 Published online by Cambridge University Press

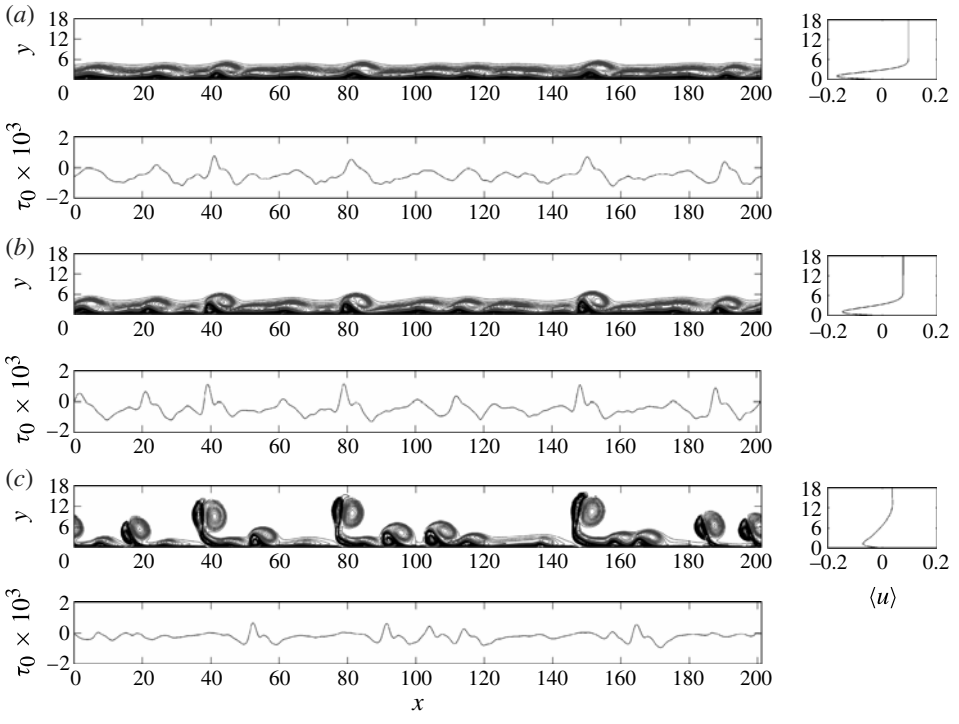


FIGURE 11. Vorticity contour, mean velocity profiles and wall shear stress τ_0 in the boundary layer under a solitary wave for $R_\delta = 748$: (*a*) $t = 4.99$, $\phi = 285.7°$ (this phase is the same as that of figure 8 of Sumer *et al.* 2010); (*b*) $t = 5.11$, $\phi = 292.78°$; (*c*) $t = 5.50$, $\phi = 315.13°$. Black lines, $\omega > 0$; grey lines, $\omega < 0$; $\Delta\omega = 0.01$.

frame 40, it can be observed that this layer is first lifted up and then it wraps around the vortex tubes, giving rise to vortex pairs.

The same description can be given for figure 12, which shows the distribution of tracers released near the bottom at the beginning of the simulation. A swirling motion of tracers can be detected a little away from the wall, indicating the presence of vortex tubes. While these vortices grow they cause the lifting of the layer of tracers adjacent to the wall, which finally wraps around the vortex tubes as shown in figure 12(*c*). If we compare figure 12(*a,b*) with figure 8 of Sumer *et al.* (2010), we observe fairly good qualitative agreement of the present results with the experiments. For instance, note the accumulation of dye particles at the foot of the vortex tubes both in the simulations and in the experiments.

With regard to the wall shear stress, in figure 11 we observe that at certain locations it reverses the sign with respect to that due to the basic flow, which is negative. For instance, in figure 11(*a,b*), in a neighbourhood of $x = 40$ the shear stress is positive. This result is due to the positive vortices generated by the roll-up of the vortex layer adjacent to the wall. Indeed, such vortices, in turn, induce negative vorticity on the wall (not clearly visible in figure 11), which consists in positive wall shear stress. Since in the boundary layer under progressive waves the vorticity dynamics is similar to the present one, there arises the issue of why an inversion of the wall shear stress is not observed in that case.

https://doi.org/10.1017/jfm.2013.274 Published online by Cambridge University Press

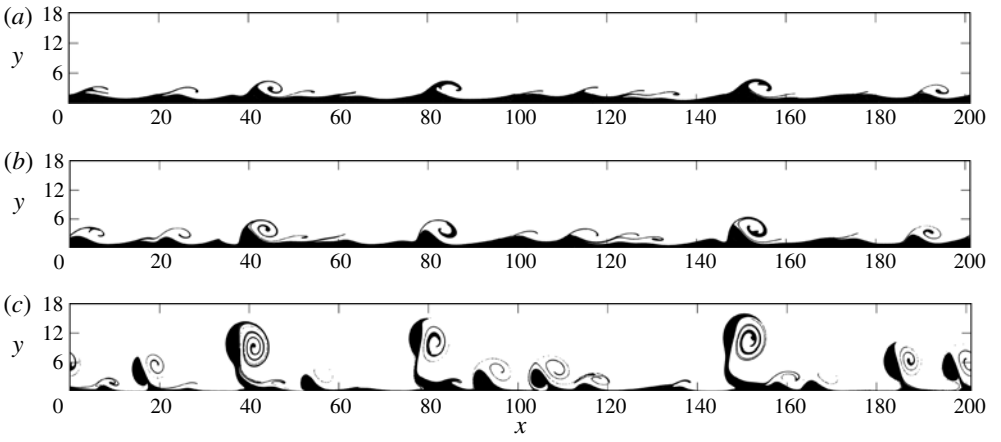


FIGURE 12. Distribution of tracers released at the beginning of the simulation in the boundary layer under a solitary wave for $R_\delta = 748$: (*a*) $t = 4.99$, $\phi = 285.7°$ (this phase is the same as that of figure 8 of Sumer *et al.* 2010); (*b*) $t = 5.11$, $\phi = 292.78°$; (*c*) $t = 5.50$, $\phi = 315.13°$.

In figures 3 and 6, where the vortices under a progressive wave are shown, the basic flow is increasing over time in the negative direction, and therefore the positive vorticity on the wall, associated with the basic flow, is also increasing. Under these circumstances the tendency of the positive vortices to generate negative vorticity on the wall is strongly hindered. Therefore, the reverse of the wall shear stress is unlikely to happen under progressive waves because of the vortex tubes. On the other hand, for the solitary wave in figure 11, the vortex tubes develop when the basic flow and the associated positive vorticity near the wall are both weak and in a decaying phase. This constitutes favourable circumstances for the positive vortices to induce negative vorticity on the wall, and therefore a reversal of the wall shear stress. We do not have a clear explanation as to why Sumer *et al.* (2010) did not observe this phenomenon.

In addition to the present case ($R_\delta = 748$, movie 2 of Sumer *et al.* 2010), we simulated three further experiments of Sumer *et al.* (2010), $R_\delta = 876$ (movie 1 of Sumer *et al.* 2010), $R_\delta = 1483$ (movie 3 of Sumer *et al.* 2010) and $R_\delta = 623$, with the aim of obtaining information on how the mean spacing between two vortex tubes depends on the Reynolds number.

The mean spacings obtained in the present simulations, expressed in terms of wavenumbers, are 0.44, 0.53, 0.47 and 0.44 for $R_\delta = 623$, 748, 876 and 1483 respectively, while those of the experiments, estimated by the same experimentalists, are 0.42, 0.49, 0.47 and 0.39. By considering the degree of subjectivity in judging the existence of a vortex tube and the different conditions that may affect the experiments and the numerical simulations, the agreement is fairly good. We observe that neither the experiments nor the numerical simulations show a monotonic trend of the wavenumber as a function of the Reynolds number. What is clear is that the wavenumbers of vortex tubes are larger than that of the most unstable mode predicted by linear stability theory ($\alpha_c = 0.36$).

With regard to the phases of inception of the vortex tubes, in the present simulations they are approximately 259, 256, 255 and 244° once again for $R_\delta = 623$, 748, 876 and 1483 respectively, while in the experiments they are 254, 237, 234 and 230°.

https://doi.org/10.1017/jfm.2013.274 Published online by Cambridge University Press

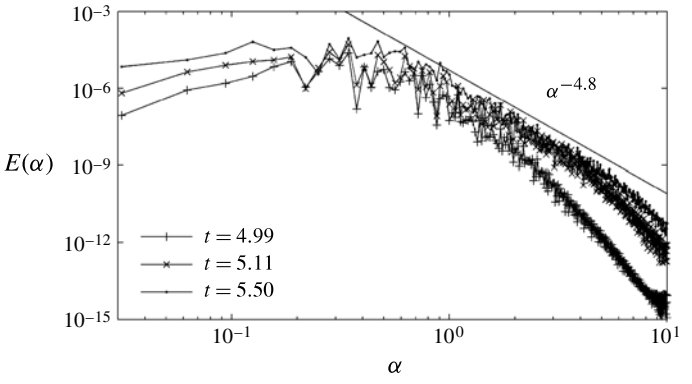


FIGURE 13. Spectra of the kinetic energy of the boundary layer under a solitary wave at different phases: $R_\delta = 748$.

Both in the experiments and in the numerical simulations the vortex tubes appear earlier when the Reynolds number increases. However, in the numerical simulations the vortex tubes appear later with respect to the experiments. A different level of ambient disturbances between experiments and numerical simulations could be one of the reasons for the discrepancy.

The longitudinal energy spectra, computed as explained in § 3, are shown in figure 13. The peak of the spectra is at about $\alpha \approx 0.35$, in agreement with the results shown in figure 10. The energy stored at low wavenumbers increases with time because of the inverse energy cascade. At large wavenumbers we observe an $\alpha^{-4.8}$ power law range, which extends for about three decades at $t = 5.50$. The steepness of the spectra is therefore smaller than that shown in figure 9 for progressive waves, but the exponent -4.8 is still large, indicating that the flow is dominated by coherent vortices.

It is interesting to compare the boundary layer flow under a progressive wave with that under a solitary wave, to show which is the most energetic. Indeed, the energy is a measure of the capability of the flow to capture the sediments that lie on the bottom and bring them into suspension. We restrict the comparison to flows characterized by identical values of the Reynolds number $R_\delta = u_0^* \delta^* / \nu^*$, where u_0^* and δ^* are defined as in § 2. The Reynolds numbers of the boundary layers under progressive and solitary waves considered here are 775 and 748, respectively. These values are sufficiently close to make appropriate the comparison between the two flows. For the comparison we consider the kinetic energy per unit mass, due to the velocity perturbations, averaged over the computational domain and made dimensionless by u_0^{*2}. This energy, here denoted by E_m, can be computed by summing the components of the spectrum, $E_m = \sum_{n=1}^{N_h} E(\alpha)$, where $\alpha = n2\pi/L_\xi$ and N_h is the number of components set equal to 350. Potentially, up to 1500 components could be considered, but we decided to truncate the spectrum as, for $n > 350$, $E(\alpha)$ is smaller than 10^{-12}. The time t_i at which the vortex tubes appear is different for the two flows, indeed $t_i \approx 9.34$ ($\phi = 175°$) for progressive waves and $t_i \approx 4.47$ ($\phi = 256°$) for solitary waves. Therefore, before comparing the energies, the origin of time is shifted in such a way that it coincides with the inception of the vortex tubes for both flows. In figure 14(*a*) we observe that the energy of the vortex tubes under solitary waves grows very rapidly and becomes larger than that under progressive waves.

https://doi.org/10.1017/jfm.2013.274 Published online by Cambridge University Press

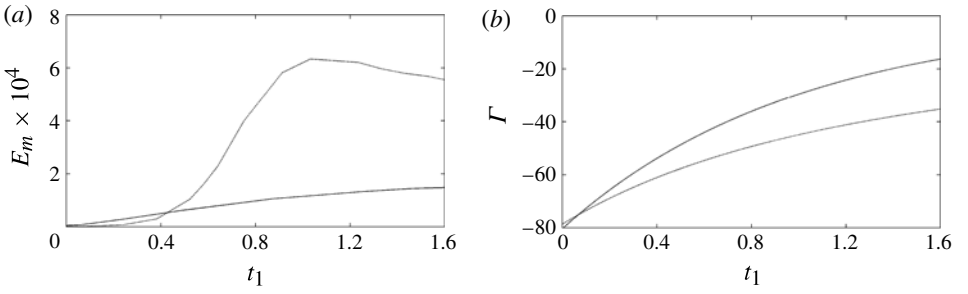


FIGURE 14. (*a*) Energy of the boundary layers; (*b*) circulation of the negative vortex layer of the basic flows. Continuous line, progressive waves; dashed line, solitary waves. The origin of the time t_1 coincides with the time of inception of the vortex tubes for both the progressive and the solitary wave.

One of the reasons for this finding may be due to a different value of the circulation of the negative vortex layer of the two flows. Indeed, since the vortex tubes gain vorticity at the expense of this layer, the higher the circulation, the larger the vortex tubes can become. Therefore, we compare the dimensionless circulation Γ of the two vortex layer, defined as follows:

$$\Gamma = \frac{\Gamma^*}{u_0^* \delta^*} = \int_C \boldsymbol{u} \cdot \boldsymbol{dl}, \tag{4.1}$$

where C is the closed line that constitutes the frontier of the vortex layer, and $\boldsymbol{dl}$ is an element of this line. In figure 14(*b*) the circulation of the negative vortex layer of the two basic flows is shown. We note that at the inception of the vortex tubes the two circulations are similar, but as the time increases the circulation for the solitary wave becomes larger, and this explains the result in figure 14(*a*).

We close this section by showing that the present flow exhibits some similarities with the laminar flow in a plane channel subject to a sudden blockage, studied in Scandura (2003), even though the two flows are subject to different constraints. Indeed, an inflection point instability develops in the channel after the sudden blockage, which causes the generation of vortices. We wish to stress that the wavelength of such vortices quantitatively agrees with those of the vortex tubes under solitary waves.

In Scandura (2003) the lengths are scaled by the distance h_p^* between the two parallel plates. Roughly speaking we can regard such a distance as twice the total thickness of the boundary layer, which can be assumed to be equal to $10\delta^*$ (see figure 11*a,b*). Therefore, the relation between the two dimensionless wavenumbers can be written as $\alpha = \alpha_s/10$. In the channel, after the flow has been suddenly blocked, the wavenumber α_s that becomes first linearly unstable is 4.16, which also characterizes the vortices generated in the nonlinear regime (Scandura 2003). By using the previous relation, this wavenumber becomes 0.416 in the present scaling, which is in fairly good agreement with those previously reported for the vortex tubes under solitary waves.

5. Conclusions

In this work the boundary layer under progressive and solitary waves has been studied with a dual purpose. On one hand we have shown that even wall imperfections of small amplitude are able to trigger boundary layer instability and lead to the

https://doi.org/10.1017/jfm.2013.274 Published online by Cambridge University Press

appearance of vortex structures. On the other hand, we have studied these vortex structures, highlighting aspects not covered in previous experimental investigations. Regarding the first objective, we have shown that the boundary layer response to wall imperfections can be important, especially in the case of solitary waves. In fact, for $R_\delta = 762$, wall imperfections of sinusoidal shape are able to trigger perturbations of $0.035u_0^*$ for progressive waves and $0.15u_0^*$ for solitary waves. These perturbations are large when compared with the slope of the wall, which is equal to 1.2×10^{-4}. Although these perturbations are large enough to suspect the presence of important nonlinear effects, the wavenumber peak of the flow response is close to that of the most unstable mode predicted by the linear theory, in the case of both progressive and solitary waves.

Numerical simulations of the vortex structures were performed on a wall characterized by random imperfections, which mimic those of a real wall. In the case of both progressive and solitary waves, vortex tubes are generated because of an inflection point linear instability of a vortex layer located a little away from the wall. After their generation the vortex tubes cause the destabilization of a second vortex layer, adjacent to the wall, characterized by vorticity opposite to that of the vortex tubes. The destabilization is due to the adverse pressure gradient induced by the vortex tubes. After the roll-up of the second vortex layer, pairs of counter-rotating vortices are generated which move away from the bottom because of the self-induced velocity.

In the case of progressive waves a decrease in the wall shear stress below each vortex tube and an increase in the region between two of them are detected. The same results are obtained in the case of a solitary wave, but the decrease is relatively large and causes the reverse of the wall shear stress.

At large wavenumbers the longitudinal energy spectra show an α^{-6} power law for progressive waves and an $\alpha^{-4.8}$ power law for solitary waves. The large exponents denote that the two flows are dominated by large coherent vortices, which survive for a long time. It is also shown that, when the Reynolds numbers of the two flows are equal, these vortices have a larger energy content for the case of a solitary wave.

The natural continuation of this work is to study the boundary layer under sea waves removing the current hypothesis of two-dimensional flow. This study may help to clarify if the vortex tubes play a role in the generation of turbulent spots and shed new light on the mechanism by which sediments are captured by the vortex structures and carried in suspension.

REFERENCES

AKHAVAN, R., KAMM, R. D. & SHAPIRO, A. H. 1991 An investigation of transition to turbulence in bounded oscillatory Stokes flows. Part 2. Numerical simulations. *J. Fluid Mech.* **225**, 423–444.

ARAKAWA, A. 1966 Computational design for long-term numerical integration of the equations of fluid motion: two-dimensional incompressible flow. Part 1. *J. Comput. Phys.* **1**, 119–143.

BATCHELOR, G. K. 1969 Computation of the energy spectrum in homogeneous two-dimensional turbulence. *Phys. Fluids Suppl. II* **12**, 233–239.

BLENNERHASSETT, P. J. & BASSOM, A. P. 2002 The linear stability of flat Stokes layers. *J. Fluid Mech.* **464**, 393–410.

BLONDEAUX, P., PRALITS, J. & VITTORI, G. 2012 Transition to turbulence at the bottom of a solitary wave. *J. Fluid Mech.* **709**, 396–407.

BLONDEAUX, P. & SEMINARA, G. 1979 Transizione incipiente al fondo di un'onda di gravità. *Lincei – Rend. Sc. Fis. Mat. e Nat.* **67**, 408–417.

BLONDEAUX, P. & VITTORI, G. 1994 Wall imperfections as a triggering mechanism for Stokes-layer transition. *J. Fluid Mech.* **264**, 107–135.

https://doi.org/10.1017/jfm.2013.274 Published online by Cambridge University Press

BRACCO, A., MCWILLIAMS, J. C., MURANTE, G., PROVENZALE, A. & WEISS, J. B. 2000 Revisiting freely decaying two-dimensional turbulence at millennial resolution. *Phys. Fluids* **12**, 2931–2941.

CARSTENSEN, S., SUMER, B. M. & FREDSØE, J. 2010 Coherent structures in wave boundary layers. Part 1. Oscillatory motion. *J. Fluid Mech.* **646**, 169–206.

DRAZIN, P. G. & REID, W. H. 2004 *Hydrodynamic Stability*. Cambridge University Press.

HALL, P. 1978 The linear stability of the flat Stokes layers. *Proc. R. Soc. Lond.* A **359**, 151–166.

HAYASHI, T. & OHASHI, M. 1982 A dynamical and visual study on the oscillatory turbulent boundary layer. In *Turbulent Shear Flows*, vol. 3, pp. 18–33. Springer.

HINO, M., SAWAMOTO, M. & TAKASU, S. 1976 Experiments on transition to turbulence in an oscillatory pipe flow. *J. Fluid Mech.* **75**, 193–207.

VON KERCZEC, C. & DAVIS, S. H. 1974 Linear stability theory of oscillatory Stokes layers. *J. Fluid Mech.* **62**, 753–773.

KRAICHNAN, R. H. 1967 Inertial ranges in two-dimensional turbulence. *Phys. Fluids* **10**, 1417–1423.

LESIEUR, M., STAQUET, C., LE ROY, P. & COMTE, P. 1987 The mixing layer and its coherence examined from the point of view of two-dimensional turbulence. *J. Fluid Mech.* **192**, 511–534.

LI, H. 1954 Stability of oscillatory laminar flow along a wall. *Tech. Rep.* 47. US Army Beach Erosion Board.

LIU, P. L.-F. & ORFILA, A. 2004 Viscous effects on transient long-wave propagation. *J. Fluid Mech.* **520**, 83–92.

LIU, P. L.-F., PARK, Y. S. & COWEN, E. A. 2007 Boundary layer flow and bed shear stress under a solitary wave. *J. Fluid Mech.* **574**, 449–463.

LUO, J. & WU, X. 2010 On the linear instability of a finite Stokes layer: instantaneous versus Floquet modes. *Phys. Fluids* **22**, 054106 (13 pages).

MAZZUOLI, M., VITTORI, G. & BLONDEAUX, P. 2011 Turbulent spots in oscillatory boundary layers. *J. Fluid Mech.* **685**, 365–376.

MERKLI, P. & THOMANN, H. 1975 Transition to turbulence in oscillating pipe flow. *J. Fluid Mech.* **68**, 567–575.

MONKEWITZ, P. A. & BUNSTER, A. 1987 The stability of the Stokes layer: visual observations and some theoretical considerations. In *Stability of Time Dependent and Spatially Varying Flows* (ed. D. L. Dwoyer & M. Y. Hussain), pp. 244–260. Springer.

OBREMSKI, H. J. & MARKOVIN, M. V. 1969 Application of a quasi-steady stability model to a periodic boundary layer flow. *AIAA J.* **7**, 1298–1301.

OHMI, M., IGUCHI, M., KALEHASHI, K. & MASUDA, T. 1982 Transition to turbulence and velocity distribution in an oscillating pipe flow. *Bull. JISME* **25**, 365–371.

SCANDURA, P. 2003 Two-dimensional perturbations in a suddenly blocked channel flow. *Eur. J. Mech.* B **22**, 317–329.

SCANDURA, P., VITTORI, G. & BLONDEAUX, P. 2000 Three-dimensional oscillatory flow over steep ripples. *J. Fluid Mech.* **412**, 355–378.

SERGEEV, S. I. 1966 Fluid oscillations in pipes at moderate Reynolds number. *J. Fluid Dyn.* **1**, 121–122.

SUMER, B. M., JENSEN, P. M., SORENSEN, L. B., FREDSØE, J., LIU, P. L.-F. & CARSTENSEN, S. 2010 Coherent structures in wave boundary layers. Part 2. Solitary motion. *J. Fluid Mech.* **646**, 207–231.

THOM, A. 1928 An investigation of fluid flow in two dimensions. *Tech. Rep.* 1194. Aerospace Research Center UK.

TROMANS, P. 1977 The stability of oscillatory pipe flow. Abstract of lecture given at Euromech 73: oscillatory flows in ducts, Aix-en-Provence, April 13–15.

VITTORI, G. & BLONDEAUX, P. 2008 Turbulent boundary layer under a solitary wave. *J. Fluid Mech.* **615**, 433–443.

https://doi.org/10.1017/jfm.2013.274 Published online by Cambridge University Press